Int J Adv Manuf Technol (2013) 67:2619–2626
DOI 10.1007/s00170-012-4678-y

ORIGINAL ARTICLE

A genuine face milling cutter geometric model for spiral bevel and hypoid gears

Shuangxi Xie

Received: 23 August 2012 / Accepted: 4 December 2012 / Published online: 24 January 2013

Abstract Accurate tooth surface and good surface quality are critical to achieve the low-noise bevel gear drives. Face milling, traditionally works as tooth roughing process, can now possibly be used for finishing process because its high speed can produce good tooth surface quality. But with the previous simplified cutter geometric model in tooth modeling, the high accurate tooth surface cannot be obtained. In this paper, a genuine face milling cutter geometric model for spiral bevel and hypoid gears is proposed. This model exactly matches with the cutter geometry in the industrial application when not considering the fabrication tolerances and tool wear . In the modeling, the blades of the genuine cutter are parameterized with blade angle, rake angles, and relief angles. The side and circular cutting edges of blades are represented on the blade rake plane, rather than the normal plane as the simplified cutter geometry. The mathematic model of the genuine tool profiles on the normal plane is derived. It can be conveniently used by the existing tooth modeling program and easily customized by specifying the geometric parameters. In comparison with the genuine tool profile with the simplified tool profile, the big geometric errors of the simplified blade profile are founded, which proves that the genuine cutter geometric model is correct and essential.

Keywords Cutter geometric model · Spiral bevel gears · Hypoid gears · Face milling

S. Xie (✉)
Department of Mechanical and Industrial Engineering,
Concordia University, Montreal, H3G 1M8 QC, Canada
e-mail: shuangxixie@gmail.com

1 Introduction

Spiral bevel and hypoid gears are massively used in automobile industry for transmission of the rotation and torque. The high quality bevel gears can work with smooth transformation, low noise, and low transmission errors. In the traditional spiral bevel and hypoid gears machining, the gear teeth are face-milled roughly, and finished by grinding, thus the finished tooth surfaces are mostly determined by the grinder profile and the machine settings. In this scenario, the face milling process has trivial effect on the accuracy of the final finished tooth surface. With the high-speed technology development in machining, the gear teeth can be ground directly from billet or face-milled up to the finished by one step. For high-speed face milling, the interrupted tool surface revolving from blade cutting edges are very close to the grinder continuous surface, thus the good tooth surface quality can be obtained as grinding. But one problem may emerge for one-step face milling. Previously, the tool surface used in tooth modeling can be easily defined from the grinder's profile, while the interrupted face milling tool surface is revolved from the cutting edges around the cutter center axis, and the cutting edges in the air may produce a more complicated tool surface, which makes its profile different with the previous tool profile definition.

Due to the specific and patented machine tool, the literature related to spiral bevel and hypoid gear manufacturing is sparse and intensively contributed by few researchers. There are two main ways to machine these complex bevel gears: face milling and face hobbing. Machining the bevel gears on general CNC machine tool is possible and cheaper for without investment on specific machine, but it is for small productivity with low efficiency and not popular as face milling and hobbing. For face milling on the bevel gear machining, Litvin and his research group [1–9] contribute

the theoretical foundation work for the modern computerized bevel gear design and manufacturing. In their work, first, the tool profile of member-gear cutter is defined, from which member-gear teeth are modeled; Second, from the curvatures at the mean point on member-gear tooth surface, the curvatures at the mean point of pinion are derived using the local synthesis; Finally, the tool profile of the pinion cutter is derived from the pinion curvatures at mean point. From this process, we can conclude that the tooth surface is mainly determined by the tool geometry and the machine settings. In their work, the cutter is defined as tool profile on the normal plane, which is correct for grinder, but may not be accurate for face milling cutter; the detail will be given in the beginning of Section 2. Simon [10, 11] modeled the cutter with an bicircular profile and an optimized diameter to obtain improved load distribution, but the profile is also defined on the cutter normal plane. Face hobbing is a continuous gear tooth generating process, unlike single indexing of the face milling process. For hobbing process, besides tool geometry and the machine settings, the tooth curvatures are also determined by the face hobbing index motion. Face milling process has higher productivity, but the grinding process cannot be applied to the tooth finishing. Previously, the hobbing cutter has been modeled with side rake angle and hook angle [12, 13], but it can be just for hobbing process.

In this work, a genuine face milling cutter geometric model for the spiral bevel and hypoid gears is proposed. The model is build up with blade geometric parameters: blade angle, rake angles, and relief angles. With this model, the cutter used in industry can be accurately represented, and also it can be easily customized. Finally, several applications are rendered to demonstrate the modeling of the genuine cutter, and compare to the previous cutter geometric model.

2 Cutter geometric model

A face milling cutter for spiral bevel and hypoid gears is composed of a group of blades, which are mounted on the cutter plates. When the blades rotate around the cutter center axis, the cutting edges of blades will generate a revolving surface, called tool surface. In the previous research, the cross section of the tool surface on normal plane is called tool profile. The normal plane could be any plane passing through the cutter center axis. For tooth grinding, the tool profile is the same as the grinder profile. The previous tool profile is modeled as two straight lines, and later, it is improved by considering the blade corners, which are modeled as two arcs (see Fig. 1). The two straight lines corresponds to the side cutting edges (SCE), which generate the gear flank; even now, the SCE is optimized as parabolic to achieve better tooth contact. The arcs corresponds to the

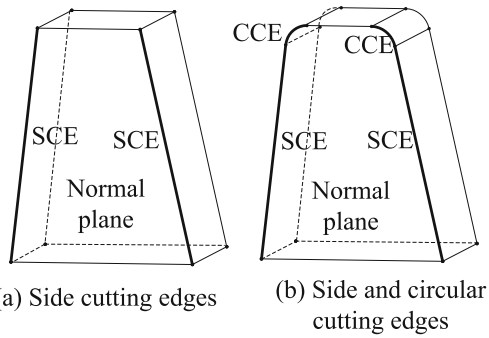

Fig. 1 Simplified blade geometric models

circular cutting edges (CCE), which generate the gear root. At the tip of the blade, the top cutting edges (TCE) generate gear tooth bottom. The gear tooth bottom is not within tooth contacting zone, thus TCE is not important as SCE and CCE in terms of geometry, although TCE is important during the material removing process. In this paper, we named the previous tool profile as simplified tool profile. The tool profile is the same as the cutting edge for simplified cutter geometric model, since both of them are defined on the normal plane.

In the industrial application, the cutting edges of the face milling blade are actually located on the blade rake face (see Fig. 2). Different companies have their own blade product. Gleason company provides several types of face milling blades, such as RIDG-AC, WEDGE-AC, HELIXFORM, RSR, SOLID, and HARDAC. These blades have their own features suiting for different cutting scenarios. In this paper, the parametric models of the blades were built up to represent the real cutting edges through analyzing the geometry of these blades (see Fig. 3). This parametric model is called as genuine blade model to differentiate from the simplified tool geometry. It includes inner blade and outer blade, which are used to generate the convex and concave gear tooth surfaces, respectively. The geometric parameters of the blades include blade angle (ϕ_c^i,ϕ_c^o), back rake angle (α_o^i, α_o^o), side rake angle (α_f^i, α_f^o), end relief angle (γ_o^i, γ_o^o), and side relief angle (γ_f^i, γ_f^o). The superscripts i and o represent the parameters of inner and outer blade, respectively. Since the geometries and modeling processes of inner blade and outer blade are similar to each other, the inner blade will be used to illustrate the modeling process in the following section.

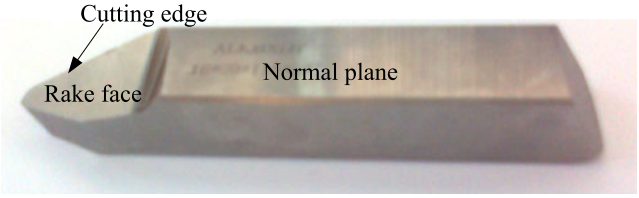

Fig. 2 Face milling blade in industrial application

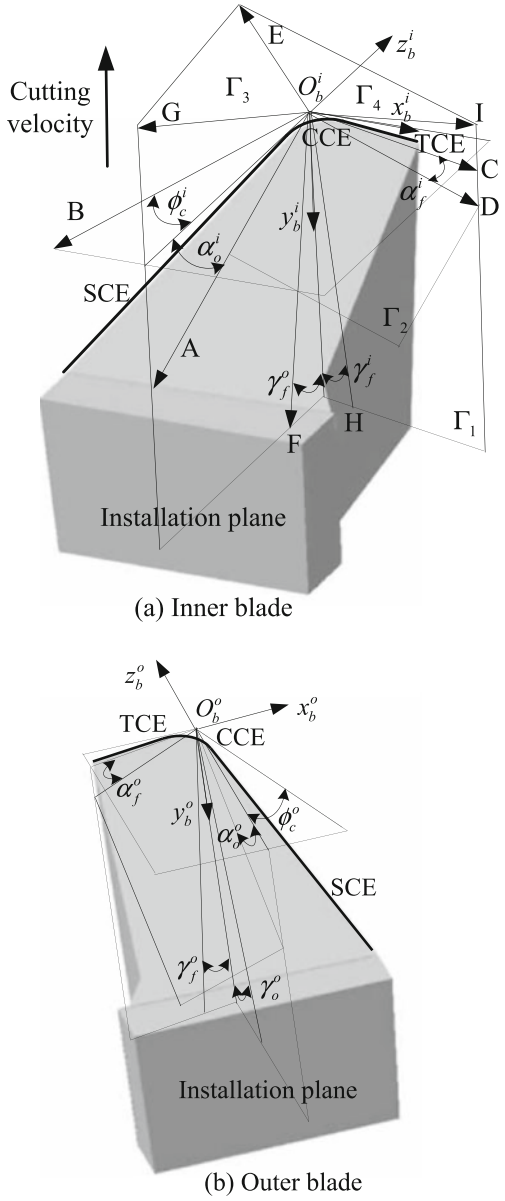

Fig. 3 Blade parametric models

2.1 Modeling the inner blade in blade coordinate system

The blade coordinate system S_b^i is set up to define the inner blade. The axis z_b^i is perpendicular to the blade installation plane, and the axis y_b^i is parallel and opposite to the cutting velocity. The axis x_b^i is the cross product of y_b^i and z_b^i by the right-hand rule (see Fig. 3). The normal plane, on which the simplified tool profiles are defined, is the same as $x_b^i z_b^i$ plane in S_b^i. For the genuine blades, their cutting edges are defined on the rake plane Γ_2, which are determined by the vectors **A** and **D**. The vector **A** is located on $y_b^i z_b^i$ plane, and forms back rake angle α_o^i with $-z_b^i$. The vector **B** is on the plane $x_b^i z_b^i$ and forms the blade angle ϕ_c^i with $-z_b^i$. The vector **C** is on the plane $x_b^i z_b^i$ and perpendicular to **B**. The plane Γ_1 is perpendicular to vector **B** and passes through the origin O_b^i. The vector **D** is on the plane Γ_1 and forms the side rake angle α_f^i with **C**. So far, **A** and **D** are determined, and both of them on the rake plane Γ_2 do cross product on vectors **A** and **D**. The normal vector **E** of Γ_2 can be derived as

$$\mathbf{E} = \begin{bmatrix} \cos\alpha_o^i \sin\alpha_f^i - \sin\alpha_o^i \cos\alpha_f^i \sin\phi_c^i \\ -\cos\alpha_o^i \cos\alpha_f^i \cos\phi_c^i \\ -\sin\alpha_o^i \cos\alpha_f^i \cos\phi_c^i \end{bmatrix} \tag{1}$$

The next step is to define the cutting edges on Γ_2. The vector **F** is on the plane $y_b^i z_b^i$ and forms the end relief angle γ_o^i with y_b^i. The vector **G** is also on $y_b^i z_b^i$ and perpendicular to **F**. The vectors **G** and **E** determine the plane Γ_3. The TCE is normal to Γ_3 and pass through O_b^i. The vector along the TCE can be derived as

$$\mathbf{C}_t^i = \begin{bmatrix} \cos\alpha_f^i \cos\phi_c^i (\cos\alpha_o^i \cos\gamma_o^i - \sin\alpha_o^i \sin\gamma_o^i) \\ \cos\gamma_o^i (\cos\alpha_o^i \sin\alpha_f^i - \sin\alpha_o^i \cos\alpha_f^i \sin\phi_c^i) \\ \sin\gamma_o^i (\sin\alpha_o^i \cos\alpha_f^i \sin\phi_c^i - \cos\alpha_o^i \sin\alpha_f^i) \\ \cdot \end{bmatrix} \tag{2}$$

The TCE is derived because it is used in the following derivative. The unit vector along TCE can be represented as $\mathbf{U}_{ct}^i$. The vector **H** is on Γ_1 and forms side relief angle γ_f^i with y_b^i. The vector **I** is on Γ_1 and perpendicular to **H**. The plane Γ_4 is determined by the vectors **I** and **E**. The SCE is normal to Γ_4 and pass through O_b^i. The vector along the TCE can be derived as

$$\mathbf{C}_s^i = \begin{bmatrix} \cos\alpha_f^i \cos\phi_c^i (\sin\alpha_o^i \sin\gamma_f^i - \cos\alpha_o^i \sin\phi_c^i \cos\gamma_f^i) \\ \cos\gamma_f^i (\cos\alpha_f^i \sin\alpha_o^i - \cos\alpha_o^i \sin\alpha_f^i \sin\phi_c^i) \\ \cos\alpha_o^i \sin\alpha_f^i \sin\gamma_f^i - \sin\alpha_o^i \cos\alpha_f^i \sin\phi_c^i \sin\gamma_f^i \\ -\cos\alpha_o^i \cos\alpha_f^i \left(\cos\phi_c^i\right)^2 \cos\gamma_f^i \end{bmatrix} \tag{3}$$

and its unit vector can be represented as $\mathbf{U}_{cs}^i$. The point width p_w describes the width of the blade tip along x_b^i, and the depth of blade d_b represents the length of the side cutting edge along z_b^i (see Fig. 4). From $\mathbf{U}_{ct}^i$ and $\mathbf{U}_{cs}^i$, the angle ϕ_a^i between them can be calculated as $\phi_a^i = \arccos(\mathbf{U}_{ct}^i \cdot \mathbf{U}_{cs}^i)$.

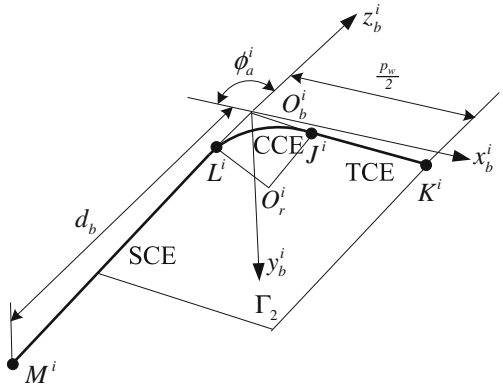

Fig. 4 Circular cutting edge of the inner blade

The TCE is the line with two ends J_i and K_i, which can be represented in S_b^i as

$$\mathbf{TCE}_b^i(u_1) = (1-u_1)J_b^i + u_1 K_b^i \quad \text{where } 0 \le u_1 \le 1 \quad (4)$$

and $J_b^i = r\cot\frac{\phi_a^i}{2}\mathbf{U}_{ct}^i$, $K_b^i = \frac{p_w}{2}\mathbf{U}_{ct}^i$. The SCE is in line with two ends L_i and M_i, which can be represented in S_b^i as

$$\mathbf{SCE}_b^i(u_2) = (1-u_2)L_b^i + u_2 M_b^i \quad \text{where } 0 \le u_2 \le 1 \quad (5)$$

and $L_b^i = r\cot\frac{\phi_a^i}{2}\mathbf{U}_{cs}^i$, $M_b^i = \frac{d_b}{Z_{\mathbf{U}_{ct}^i}}\mathbf{U}_{cs}^i$.

So far, the TCE and SCE are determined; the next step is to define the CCE (see Fig. 4). The CCE is an arc on the rake plane Γ_2. It is tangent to TCE and SCE with radius r, and can be obtained by transforming an arc with radius r from $x_b^i z_b^i$ plane to Γ_2 plane. Finally, it can be represented in S_b^i as

$$\mathbf{CCE}_b^i(\phi^i) = \begin{bmatrix} r\cos\phi_b^i\cos\phi^i + X_{O_{br}^i} \\ r\cos\alpha_o^i\sin\phi_b^i\cos\phi^i - r\sin\alpha_o^i\sin\phi^i + Y_{O_{br}^i} \\ r\sin\alpha_o^i\sin\phi_b^i\cos\phi^i + r\cos\alpha_o^i\sin\phi^i + Z_{O_{br}^i} \\ , \end{bmatrix} \quad (6)$$

where $0 \le \phi^i \le \frac{\pi}{2} - \phi_a^i$, and here $[X_{O_{br}^i} \quad Y_{O_{br}^i} \quad Z_{O_{br}^i}]^T$ are the coordinates of the point O_r^i in S_b^i. It can be calculated from the equation

$$O_{br}^i = r\cot\frac{\phi_a^i}{2}\mathbf{U}_{ct}^i + r(\mathbf{U}_{ct}^i \times \mathbf{U}_E), \quad (7)$$

and $\phi_b^i = \arcsin(\frac{X_E}{\sqrt{(X_E)^2+(Y_E)^2+(Z_E)^2}})$. Using the similar procedure, the cutting edges of outer blade $\mathbf{SCE}_b^o$, $\mathbf{CCE}_b^o$, and $\mathbf{TCE}_b^o$ can also be derived.

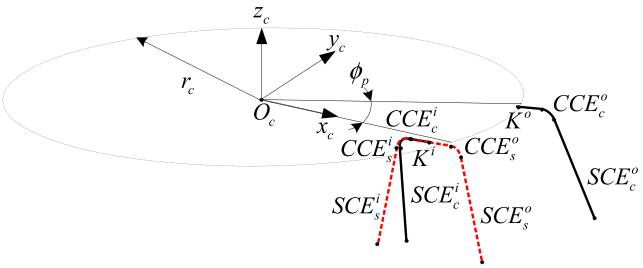

Fig. 5 Blades in cutter coordinate system

2.2 Blades in the cutter coordinate system

The inner and outer blades are mounted on the cutter plates alternating. Figure 5 shows their position in the cutter coordinate system S_c. The average radius r_c represents the distance of the blades to the cutter center axis, and the pitch angle ϕ_p describes the angle between two adjacent blades. SCE_c^i and SCE_c^o are the side cutting edges of genuine inner and outer blades. CCE_c^i and CCE_c^o are the circular cutting edges of genuine inner and outer blades. SCE_s^i, SCE_s^o, CCE_s^i, and CCE_s^o are the side and circular cutting edges of the simplified inner and outer blades.

The cutting edges of inner blade can be transformed from S_b^i to S_c by the equations $[SCE_c^i \ 1]^T = M_{cb}^i \cdot [SCE_b^i \ 1]^T$ and $[CCE_c^i \ 1]^T = M_{cb}^i \cdot [CCE_b^i \ 1]^T$, with the matrix

$$M_{cb}^i = \begin{bmatrix} 1 & 0 & 0 & \sqrt{(r_c)^2 - (Y_{K_b^i})^2} - X_{K_b^i} \\ 0 & 1 & 0 & 0 \\ 0 & 0 & 1 & 0 \\ 0 & 0 & 0 & 1 \\ . & & & \end{bmatrix}$$

The coordinates of point K^i has been derived in the previous section. With the similar process, the cutting edges of outer blade can be transformed from outer blade coordinate system to S_c by the equations $[SCE_c^o \ 1]^T = M_{cb}^o \cdot [SCE_b^o \ 1]^T$ and $[CCE_c^o \ 1]^T = M_{cb}^o \cdot [CCE_b^o \ 1]^T$, with the matrix

$$M_{cb}^o = \begin{bmatrix} \cos\phi_p & -\sin\phi_p & 0 & \sqrt{(r_c)^2 - (Y_{K_b^o})^2} - X_{K_b^o} \\ \sin\phi_p & \cos\phi_p & 0 & 0 \\ 0 & 0 & 1 & 0 \\ 0 & 0 & 0 & 1 \end{bmatrix}.$$

3 Genuine tool profile on normal plane

The equations of genuine cutting edge in S_c are derived above. The tool surfaces can be obtained by rotating them around the cutter center axis z_c. After the cross section of tool surfaces on normal plane is taken, the genuine tool profile is acquired. Due to the similar derivative processes of

inner and outer blades, here, the tool profile of inner blade is derived as demonstrated.

3.1 Genuine tool profile corresponding to inner blade SCE

Figure 6 shows the SCE of genuine inner blade with two ends L^i and M^i on the rake plane. Their coordinates in S_c can be calculated from equations $[L_c^i \quad 1]^T = M_{cb}^i \cdot [L_b^i \quad 1]^T$ and $[M_c^i \quad 1]^T = M_{cb}^i \cdot [M_b^i \quad 1]^T$. When it rotates around the axis z_c , the generated tool surface can be represented as

$$\mathbf{T}_{SCE}^i(u_2,\theta^i) = \begin{bmatrix} \cos\theta^i[X_{L_c^i} + u_2(X_{M_c^i} - X_{L_c^i})] \\ \quad -\sin\theta^i[Y_{L_c^i} + u_2(Y_{M_c^i} - Y_{L_c^i})] \\ \sin\theta^i[X_{L_c^i} + u_2(X_{M_c^i} - X_{L_c^i})] \\ \quad +\cos\theta^i[Y_{L_c^i} + u_2(Y_{M_c^i} - Y_{L_c^i})] \\ Z_{L_c^i} + u_2(Z_{M_c^i} - Z_{L_c^i}) \end{bmatrix}, \tag{8}$$

where $0 \le u_1 \le 1$, $0 \le \theta^i \le 2\pi$. The tool profile on normal plane should satisfy the equation $Y_{T_{SCE}^i} = 0$. With this equation, the tool profile $\widehat{L_p^i M_p^i}$ corresponding to SCE of inner blade can be derived explicitly as

$$\frac{x^2}{a^2} - \frac{(z-c)^2}{b^2} = 1 \tag{9}$$

with the parameters

$$a = \sqrt{(X_{L_c^i})^2 + (Y_{L_c^i})^2 - \frac{[X_{L_c^i}(X_{M_c^i} - X_{L_c^i}) + Y_{L_c^i}(Y_{M_c^i} - Y_{L_c^i})]^2}{(X_{M_c^i} - X_{L_c^i})^2 + (Y_{M_c^i} - Y_{L_c^i})^2}}$$

$$b = (Z_{M_c^i} - Z_{L_c^i})\sqrt{(X_{L_c^i})^2 + (Y_{L_c^i})^2} \cdot \frac{\sqrt{(X_{M_c^i} - X_{L_c^i})(X_{M_c^i} - 2X_{L_c^i}) + (Y_{M_c^i} - Y_{L_c^i})(Y_{M_c^i} - 2Y_{L_c^i})}}{(X_{M_c^i} - X_{L_c^i})^2 + (Y_{M_c^i} - Y_{L_c^i})^2}$$

$$c = Z_{L_c^i} - \frac{(Z_{M_c^i} - Z_{L_c^i})[X_{L_c^i}(X_{M_c^i} - X_{L_c^i}) + Y_{L_c^i}(Y_{M_c^i} - Y_{L_c^i})]}{(X_{M_c^i} - X_{L_c^i})^2 + (Y_{M_c^i} - Y_{L_c^i})^2}.$$

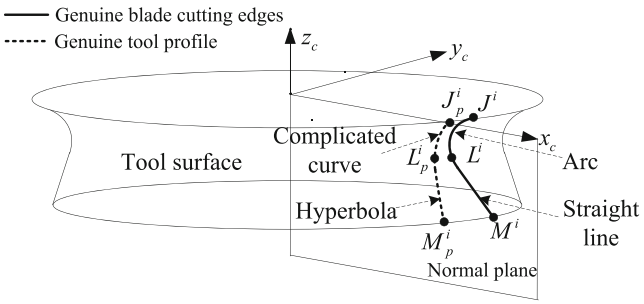

Fig. 6 Genuine inner tool profile

This is a hyperbola curve. It is different with the simplified profile corresponding to SCE, which is a straight line on the normal plane.

3.2 Genuine tool profile corresponding to inner blade CCE

Figure 6 shows the CCE of inner blade with two ends L^i and J^i. When it rotates around the axis z_c, the generated tool surface can be represented as

$$\mathbf{T}_{CCE}^i(\phi^i,\theta^i) = \begin{bmatrix} \cos\theta^i X_{CCE_c^i}(\phi^i) - \sin\theta^i Y_{CCE_c^i}(\phi^i) \\ \sin\theta^i X_{CCE_c^i}(\phi^i) + \cos\theta^i Y_{CCE_c^i}(\phi^i) \\ Z_{CCE_c^i} \\ , \end{bmatrix} \tag{10}$$

where $0 \le \phi^i \le \frac{\pi}{2} - \phi_a^i$, $0 \le \theta^i \le 2\pi$. The tool profile on normal plane should satisfy the equation $Y_{T_{CCE}^i} = 0$. With this equation, the tool profile of CCE on the normal plane can be found, which can be represented as

$$\widehat{L_p^i M_p^i}(\phi^i) = \begin{bmatrix} a_2(r\cos\phi_b\cos\phi^i + X_{O_{cr}^i}) \\ -a_1(r\cos\alpha_o^i\sin\phi_b\cos\phi^i - r\sin\alpha_o^i\sin\phi^i + Y_{O_{cr}^i}) \\ r\sin\alpha_o^i\sin\phi_b\cos\phi^i + r\cos\alpha_o^i\sin\phi^i + Z_{O_{cr}^i} \end{bmatrix}, \tag{11}$$

where $0 \le \phi^i \le \frac{\pi}{2} - \phi_a^i$ and $[X_{O_{cr}^i} \quad Y_{O_{cr}^i} \quad Z_{O_{cr}^i}]^T$ are the coordinates of origin O_r^i in S_c, which can be calculated from equations $[O_{cr}^i \quad 1]^T = M_{cb}^i \cdot [O_{br}^i \quad 1]^T$. The parameters a_1 and a_2 are

$$a_1 = \frac{-Y_{CCE_c^i}}{\sqrt{(X_{CCE_c^i})^2 + (Y_{CCE_c^i})^2}}$$

and

$$a_2 = \frac{X_{CCE_c^i}}{\sqrt{(X_{CCE_c^i})^2 + (Y_{CCE_c^i})^2}}.$$

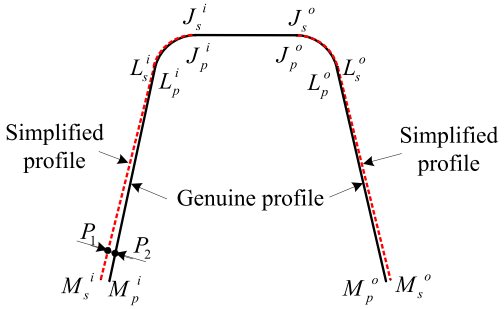

Fig. 7 Geometric errors of the simplified cutter

Table 1 Geometric parameters of the cutter

Geometric parameters	Inner blade	Outer blade
Bake rake angle (deg)	20	20
End relief angle (deg)	12	12
Side rake angle (deg)	10	10
Side relief angle (deg)	4	4
Inner blade angle (deg)	20.5	20.5
Outer blade angle(deg)	22.5	22.5
Depth of blade (mm)	17.8	17.8
Corner radius (mm)	1	1
Point width (mm)	2.54	2.54

This results show the tool profile corresponding to CCE is a complicated curve. It is different with the simplified profile corresponding to CCE, which is an arc on normal plane.

4 Geometric error of simplified cutter model

Since the genuine and simplified tool surfaces are both revolving surfaces around the cutter center axis, the geometric error of the tool surfaces of the simplified blade can be evaluated by comparing its tool profile with the genuine tool profile. In Fig. 7, the curves $\overline{L_s^i M_s^i}$, $\overline{L_s^o M_s^o}$, $\widehat{L_s^i J_s^i}$, and $\widehat{L_s^o J_s^o}$ are the inner and outer SCE, and inner and outer CCE of simplified cutter, respectively. $\widehat{L_p^i M_p^i}$ and $\widehat{L_p^i J_p^i}$ are the genuine profiles corresponding to the SCE and CCE of inner blade. $\widehat{L_p^o M_p^o}$ and $\widehat{L_p^o J_p^o}$ are the genuine profiles corresponding to the SCE and CCE of outer blade. Assume one point P_1 is on the simplified profile, one nearest point P_2 on the genuine tool profile can be found. The geometric error at point P_1 can be represented as

$$error = |P_2 - P_1| \tag{12}$$

5 Applications

To verify the models proposed above, several experiments are conducted. First experiment is to test how big are the geometric errors for one pair of blades. The geometric parameters of the blades used in test are presented in Table 1. The average cutter radius is 152.8 mm. To show the effect of the distance to cutter center of blades on the geometric error, the same parameter values are used for inner and outer blade. In this example, first, the cutting edges of the inner and outer blade are modeled with parameters from Table 1. Then the tool surfaces are determined by revolving the cutting edges, and the genuine tool profiles are obtained by taking the cross section on normal plane of the tool surfaces (see Fig. 8). To evaluate the geometric error of the simplified cutter, the simplified tool profiles are also build up without considering the rake and relief angles. Figure 8 shows that there are obvious distances between the profile of simplified and genuine profile from both inner and outer sides. The geometric errors of simplified inner blade and outer blade along profile are calculated (see Fig. 9). Since the surface generated by TCE will not affect the mating of pair of gears, only the errors of the SCE and CCE are analyzed. From Fig. 9 it can be observed that the geometric errors from blade tip to bottom are gradually increasing. At the same height in z_c direction the geometric errors of inner blade are larger than the errors of outer blade because the distance of outer blade to the cutter center is larger than the distance of inner blade to the cutter center. At the depth of blade given in the table, the maximum geometric error of the simplified inner profile is about 0.53 mm, and the maximum geometric error of the simplified outer profile is about 0.32 mm. Since not all the cutting edge segments in the machining process participate in the material removal, we care more about the geometric error at the mean point. The geometric error at the mean point of the inner simplified profile is about 0.21 mm, and the geometric error at the mean point of the outer simplified profile is about 0.17 mm.

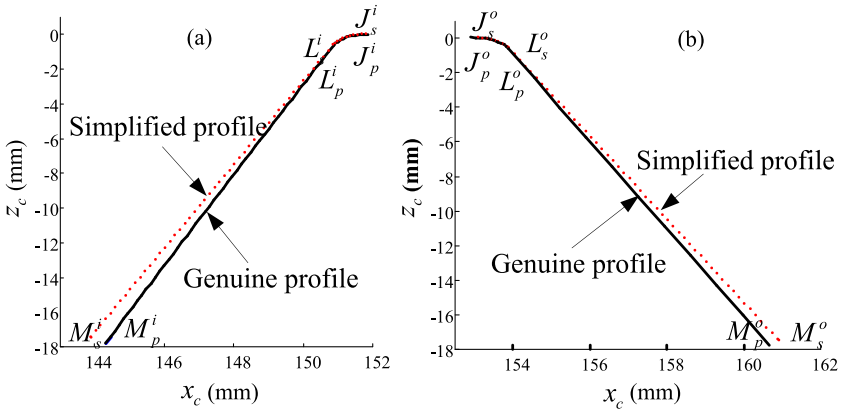

Fig. 8 Profiles of the blades: **a** inner blade, **b** outer blade

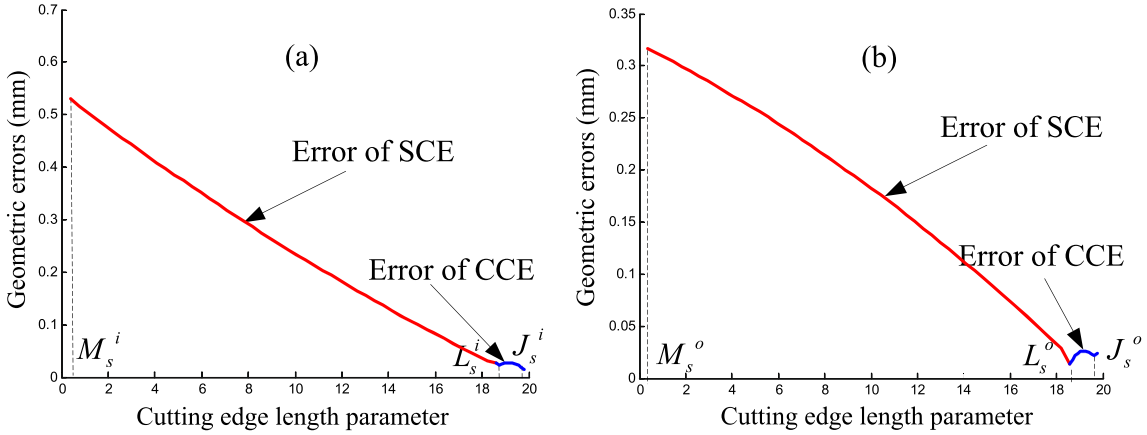

Fig. 9 Geometric errors of the simplified profiles: **a** inner blade, **b** outer blade

The second experiment is to test the different effects of the geometric parameters on the errors (see Fig. 10). In the following tests, all the geometric errors are calculated at the mean point. In test (a) the same geometric parameters as those in the first experiment are used except the back rake angles varies from 0° to 20°. Figure 10 shows that with the back rake angle increasing, the geometric errors decrease at the beginning and then gradually increase. The minimum errors of inner and outer blade are both about 0.007 mm. The maximum error for inner blade is about 0.21 mm, and for out blade, it is about 0.17 mm. In test (b) the side rake angles vary from 0° to 10°. The result shows that with the side rake angle changing, the geometric errors almost keep constant. In test (c), the end relief angles vary from 0° to 10°. The result shows with the end relief angle increasing, the geometric errors of inner blade keep on increasing from 0.02

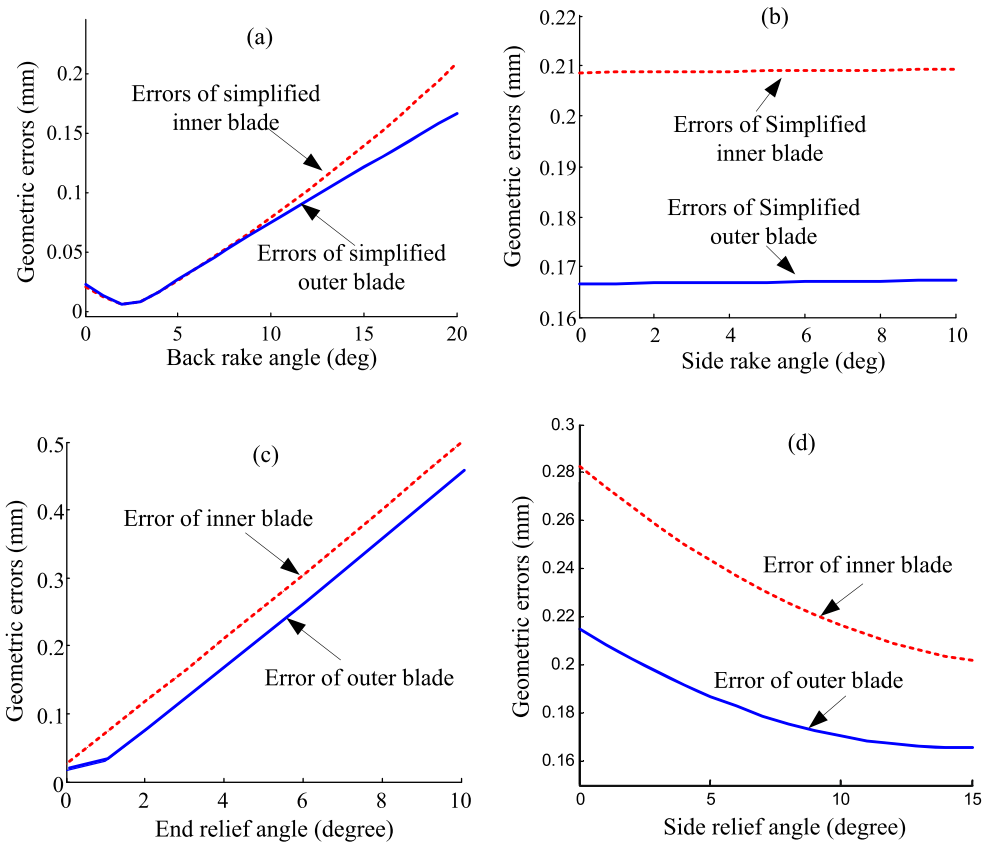

Fig. 10 Geometric errors with parameter varying: **a** back rake angle, **b** side rake angle, **c** end relief angle, and **d** side relief angle

to 0.50 mm, and the errors of outer blade increases from 0.01 to 0.45 mm. In test (d), the side relief angles vary from 0° to 15°. It shows that with the side relief angle increasing, the geometric errors of inner blade gradually decrease from 0.28 to 0.20 mm, and the errors of outer blade decrease from 0.21 to 0.16 mm. The tests shows that the geometric errors of the simplified cutter is too big referred to the accuracy requirement, thus they cannot be neglected during the tooth modeling. The tests also shows the different geometric parameters have different effect on the accuracy of tool profile, big geometric error will produce if the back rake angle and end relief angle are omitted in the cutter modeling. The genuine cutter geometric model can provide the exact same cutting edges as cutter in industrial application; with this model, it becomes possible for the following accurate gear tooth modeling.

6 Conclusion

In this paper, a genuine cutter geometric model of face-milled spiral bevel and hypoid gears is proposed. This geometric model is build up as following the real cutter geometry in industrial applications. During the modeling, the geometric parameters including rake angles and relief angles are taken into consideration. The cutting edges are accurately represented on the rake plane, and the tool profiles on normal plane are mathematically derived. The cutter can be easily customized by modifying the blade geometric parameters, and easily used for the following gear tooth modeling. In the final applications, the results show that the geometric errors of the simplified cutter are too big referring to the accuracy requirement, thus it cannot be neglected. The genuine cutter geometric model lays down a ground for the high speed face milling used for gear tooth finishing, which asks for high accuracy and good surface quality.

References

1. Litvin FL, Gutman Y (1980) Methods of synthesis and analysis for hypoid gear-drives of “formate” and “helixform”—Part 1. Calculations for machine settings for member gear manufacture of the formate and helixform hypoid gears. J Mech Des 103:83–88
2. Litvin FL, Gutman Y (1980) Methods of synthesis and analysis for hypoid gear-drives of “formate” and “helixform”—Part 2. Machine setting calculations for the pinion of formate and helixform gears. J Mech Des 103:89–101
3. Litvin FL, Gutman Y (1980) Methods of synthesis and analysis for hypoid gear-drives of “formate” and “helixform”—Part 3. Analysis and optimal synthesis methods for mismatch gearing and its application for hypoid gears of formate and helixform. J Mech Des 103:102–113
4. Zhang Y, Litvin FL, Handschuh RF (1995) Computerized design of low-noise face-milled spiral bevel gears. Mech Mach Theory 30:1171–1178
5. Litvin FL, Wang AG, Handschuh RF (1998) Computerized generation and simulation of meshing and contact of spiral bevel gears with improved geometry. Comput Methods Appl Mech Eng 158:35–64
6. Argyris J, Fuentes A, Litvin FL (2002) Computerized integrated approach for design and stress analysis of spiral bevel gears. Comput Methods Appl Mech Eng 191:1057–1095
7. Fuentes A, Litvin FL, et al (2002) Design and stress analysis of low-noise adjusted bearing contact spiral bevel gears. J Mech Des 124:524–532. doi:10.1115/1.1481364
8. Litvin FL, Fuentes A, Fan Q, Handschuh RF (2002) Computerized design, simulation of meshing, and contact and stress analysis of face-milled formate generated spiral bevel gears. Mech Mach Theory 37:441–459
9. Litvin FL, Fuentes A, Hayasaka K (2006) Design, manufacture, stress analysis, and experimental tests of low-noise high endurance spiral bevel gears. Mech Mach Theory 41:83–118
10. Simon V (2009) Head-cutter for optimal tooth modifications in spiral bevel gears. Mech Mach Theory 44:1420–1435
11. Simon V (2005) Optimal tooth modification in hypoid gears. J Mech Des 127:646–655. doi:10.1115/1.1899177
12. Fan Q (2010) Tooth surface error correction for face-hobbed hypoid gears. J Mech Des 132(1–8):011004. doi:10.1115/1.4000646
13. Fan Q (2006) Computerized modeling and simulation of spiral bevel and hypoid gears manufactured by Gleason face hobbing process. J Mech Des 128:1315–1327. doi:10.1115/1.2337316